Pocket vibrational modes in crystals: Theory and experiment

K. W. Sandusky
Department of Physics and Astronomy, Arizona State University, Tempe, Arizona 85287-1504

J. B. Page
Department of Physics and Astronomy, Arizona State University, Tempe, Arizona 85287-1504 and Institute for Theoretical Physics, University of Regensburg, DW-8400 Regensburg, Germany*

A. Rosenberg and A. J. Sievers
Laboratory of Atomic and Solid State Physics and Materials Science Center, Cornell University, Ithaca, New York 14853-2501
(Received 14 August 1992)

A perturbed-shell-model calculation for the $T=0$ K on-center dynamics of the thermally unstable impurity system KI:Ag^+ predicts three nearly degenerate localized gap modes of different symmetry with highly unusual displacement patterns: the displacements are peaked on the defect's fourth-nearest neighbors, with negligible displacements on the defect or its nearest neighbors. The model predictions are in good agreement with far-infrared isotope-effect measurements, providing a direct confirmation of the existence of these "pocket" modes. We also discuss an experimental technique that yields a major reduction in the uncertainties in the measured temperature dependence of the absorption strength due to the infrared-active pocket mode. As a result, we show that the previously observed disappearance of this mode's absorption between 1.2 and 25 K occurs with exactly the same temperature dependence as that of a low-frequency resonant mode whose displacements are instead localized at the impurity and its nearest neighbors. This result, together with the calculated displacement patterns of the pocket and resonant modes, indicates that the anomalous thermally driven (on→off)-center transition of the Ag^+ impurity in KI involves the entire coupled defect-host system around the impurity.

I. INTRODUCTION

Impurity-induced localized modes with frequencies outside the host-crystal phonon bands and displacement patterns peaked at or adjacent to the impurity have been investigated since the 1960's.[1-3] However, a recent theoretical and experimental study of isotope-induced infrared (IR) absorption spectra of KI:Ag^+ has confirmed the existence of a strikingly different type of localized vibrational mode, whose displacement patterns are strongly peaked in regions of the crystal well *away* from the Ag^+.[4] In this paper, we present a more thorough discussion of both the theoretical and experimental aspects of the confirmation of these localized "pocket" modes. We review the theoretical methods used to calculate the pocket mode displacement patterns and IR spectra, and we show that pocket modes are a general feature of a class of lattice-defect systems in ionic crystals. In addition, we present experimental techniques that provide a greatly improved determination of the temperature dependence of the pocket modes' IR absorption strengths in KI:Ag^+. As a result, this joint theoretical-experimental study provides important information for understanding the anomalous thermal properties of this unusual defect system.

KI:Ag^+ is the most thermally unstable lattice-defect system known. Far-IR,[5] radio-frequency,[6] Raman,[7] and UV (Ref. 7) measurements all show that as the temperature is raised from 1.2 to 25 K the system undergoes a transition from an on-center configuration, in which the Ag^+ ion occupies a normal host-crystal K^+ site, to an as yet incompletely determined off-center configuration. As the crystal is heated, the strengths of the impurity-induced IR and Raman peaks simply vanish, with little shifting or broadening. The on-center spectroscopic transitions disappear with increasing temperature at a rate much faster than can be explained by population effects associated with just the Ag^+ ion moving off center in a static potential well, indicating that the high-temperature off-center configuration has a very large number of available states.

Surprisingly, this system's low-temperature on-center dynamics are consistent with a perturbed *harmonic* shell model.[7] In this model, which involves substantial force-constant softening, the Ag^+ impurity is characterized by its mass and by assumed impurity–first-neighbor and relaxation-induced first-neighbor–fourth-neighbor longitudinal force-constant changes. These two force-constant changes are fit to the observed impurity-induced T_{1u} in-band resonant mode and localized gap-mode IR frequency peaks at 17.3 and 86.2 cm^{-1}, respectively. All other long- and short-range force constants are assumed to be unperturbed, and are included via the use of realistic breathing shell-model phonons to compute the necessary harmonic Green's functions. The computed relative strengths for the IR absorption of the T_{1u} resonant and gap modes are in reasonable agreement with experiment, and the model predicts a Raman-active E_g resonant mode at 20.5 cm^{-1}, in good agreement with the observed E_g Raman peak at 16.1 cm^{-1}.[7,8]

In addition to the threefold-degenerate T_{1u} gap mode at 86.2 cm^{-1}, our model also predicts a twofold-degenerate E_g gap mode at 86.0 cm^{-1} and a nondegenerate A_{1g} gap mode at 87.2 cm^{-1}. The three gap modes have some unusual properties. First, despite their different symmetries, the frequencies are very nearly degenerate. Second, the computed displacement patterns for all three modes are strongly localized on the defect's fourth-neighbor [e.g., (200)] potassium ions, away from the Ag^+ impurity and its nearest neighbors. This is in sharp contrast to the usual localized or resonant-mode behavior, in which the displacement patterns are peaked at or adjacent to the defect. Figures 1(a)–1(c) show our computed displacement patterns for gap modes of all three symmetry types. For comparison, Fig. 1(d) also shows the displacement pattern for the 17.3-cm^{-1} T_{1u} resonant mode, which is seen to be peaked on the impurity and its nearest neighbors. In contrast, the three gap modes consist of very similar isolated pockets of displacements on the (200) family of K^+ ions; hence the name pocket modes. The near degeneracy of these modes indicates that the frequencies are mainly determined by the local dynamics within each pocket, with the pockets being weakly coupled to produce the different symmetry modes.

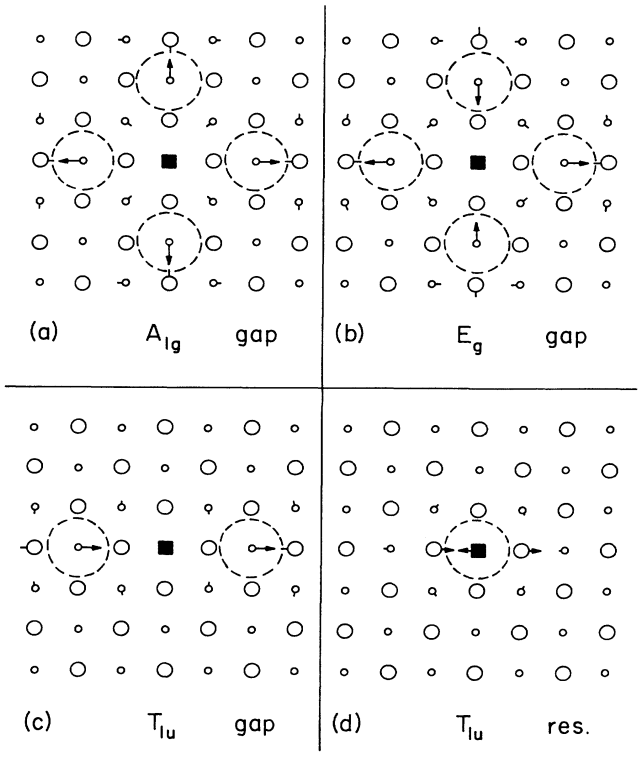

FIG. 1. Calculated displacement patterns for different KI:Ag^+ impurity modes. (a) 87.2-cm^{-1} A_{1g} pocket gap mode. (b) 86.0-cm^{-1} E_g1 pocket gap mode. (c) 86.2-cm^{-1} $T_{1u}x$ pocket gap mode. (d) 17.3-cm^{-1} $T_{1u}x$ resonant mode. Here $T_{1u}x$ denotes the T_{1u} partner which couples to x-polarized radiation, and E_g1 denotes one of two degenerate E_g partners. For our choice of partners, parts (a), (c), and (d) show displacements in the x-y plane, while (b) shows displacements in the y-z plane. Note that the displacement pattern for the resonant mode is peaked on the defect and its nearest neighbors, while the displacement patterns for the pocket gap modes (a)–(c) are peaked on the fourth-neighbor sites, away from the defect. The displacements are given in arbitrary units. See Ref. 14.

The even-parity A_{1g} and E_g pocket modes should be Raman active. However, our model predicts that their Raman strengths would be too weak to observe; indeed, no evidence for these modes was found in Raman experiments.[7] Another way to directly confirm the existence of these unusual modes is provided by the natural occurrence of a 7% isotopic abundance of $^{41}K^+$ in the host KI crystal. The presence of $^{41}K^+$ isotopes on the Ag^+ impurity's fourth-nearest neighbors strongly mixes the pocket modes of all three symmetry types. Using nearly degenerate perturbation theory within our model, together with a calculation of the probabilities of the possible impurity-isotope configurations, we predict an observable "isotope pocket mode," whose frequency and intensity are in good agreement with our high-resolution IR measurements. Alternative explanations of the data in terms of Ag^+ isotopes, or of isolated pocket modes of a single symmetry type, are shown to fail.

With the existence of the pocket modes in KI:Ag^+ having thus been directly established, it becomes important to reexamine the temperature dependence of the IR spectra for the T_{1u} low-frequency resonant and pocket gap modes as the system undergoes the thermally driven (on→off)-center transition, because these modes' displacement patterns are localized in different spatial regions. In our previously reported measurements,[4] the temperature dependence was found to be the same for these two modes within the experimental uncertainties. Unfortunately, these uncertainties were much more pronounced for the gap mode, due to the presence of a temperature-dependent background produced by intrinsic difference-band absorption. To circumvent this problem, we have employed a rapid-scanning interferometer to obtain accurate measurements of the *derivative* of the far-IR absorption spectra. Because of the resulting enhanced contrast for sharp spectral features, we are able to conclude that the low-frequency resonant mode and the pocket-gap-mode IR absorption strengths disappear with *identical* temperature dependences. Hence, the (on→off)-center transition involves not just the impurity moving in a static host lattice, but rather the entire coupled defect-host system in the impurity region.

The remainder of the paper is organized as follows. The theory and numerical calculation are presented in Sec. II. In Secs. II A and II B, we review the Lifshitz method used in our calculation of the perturbed harmonic dynamics. From the resulting expressions, we determine both the normalized gap-mode displacement patterns and the IR absorption. In Sec. II C, we discuss our impurity model for the low-temperature dynamics of KI:Ag^+. The theory and numerical results of our isotope-mode calculations are presented in Sec. II D. The experiments are described in Sec. III. In Sec. III A, the gap-region experiments are presented and the isotope-

shifted pocket mode is identified. In Sec. III B, data analyses of the gap-mode strengths are detailed, including the derivative measurements for the temperature dependence. The theoretical and experimental results are discussed in Sec. IV. A summary of the main conclusions is given in Sec. V, together with some additional discussion.

II. THEORY

A. Local modes

The Lifshitz harmonic Green's-function method for computing general defect-phonon properties is detailed in Refs. 1 and 3. For completeness, we sketch here our application of this method to determine the frequencies, displacement patterns, and IR spectra of localized modes arising from substitutional impurities. We assume low enough defect concentrations that the strengths of the experimental spectra scale linearly with concentration; this holds well for KI:Ag^+ and allows us to treat the case of just a single impurity.

For a system of N ions interacting via harmonic forces, the normal-mode frequencies $\{\omega_f\}$ and displacements $\chi(f)=\{\chi_\alpha(l|f)\}$ are determined by the $3N\times 3N$ matrix eigenvalue equation

$$(\Phi-\omega_f^2 M)\chi(f)=\mathbf{0}\ , \tag{1}$$

where the $\Phi=\{\Phi_{\alpha\beta}(l,m)\}$ is the harmonic force-constant matrix, $M=\{M(l)\delta_{\alpha\beta}\delta_{lm}\}$ is the diagonal mass matrix, and $f=1,\ldots,3N$ labels the modes. The ion sites are labeled by $l,m=1,\ldots,N$, while $\alpha,\beta=x,y,z$ denote Cartesian components. The force-constant matrix is symmetric ($\tilde{\Phi}=\Phi$), and the modes are normalized such that the orthonormality relation is $\tilde{\chi}(f)M\chi(f')=\delta_{ff'}$. With a substitutional defect present, it is convenient to rewrite Eq. (1) identically in terms of the host-crystal harmonic Green's-function matrix $G_0(\omega^2)=(\Phi_0-\omega^2 M_0)^{-1}$ and the perturbing matrix $C(\omega^2)=\Delta\Phi-\omega^2\Delta M$, containing the impurity-induced force constant and mass changes. The result is

$$[I+G_0(\omega_f^2)C(\omega_f^2)]\chi(f)=\mathbf{0}\ . \tag{2}$$

This equation can be partitioned into two equations: one involving just components inside the defect space, defined by the sites associated with nonzero elements of C, and a second which determines the mode displacements outside the defect space:

$$[I_{II}+G_{0II}(\omega_f^2)C_{II}(\omega_f^2)]\chi_I(f)=\mathbf{0} \tag{3}$$

and

$$\chi_R(f)=-G_{0RI}(\omega_f^2)C_{II}(\omega_f^2)\chi_I(f)\ . \tag{4}$$

The subscripts I and R refer to components inside and outside the defect space, respectively. Equation (3) gives the determinental frequency condition

$$|I_{II}+G_{0II}(\omega_f^2)C_{II}(\omega_f^2)|=0\ . \tag{5}$$

For isoelectronic impurities, the defect space is usually small. Equation (5) then involves the determinant of a small matrix and is thus practicable, provided the defect-space elements of the unperturbed harmonic Green's-function matrix can be computed. As will be outlined in Sec. II C, this is readily done for localized modes by direct summations involving the unperturbed host-crystal phonons; for alkali halides, these are well known through phenomenological models (e.g., shell models) that account very well for the measured phonon-dispersion curves. Once the local-mode frequency is known, Eq. (3) can be used to compute the defect-space displacement pattern, to within a normalization constant. The displacements outside the defect space may then be determined by Eq. (4).

Equations (3) and (4) determine the *relative* displacements for a local mode. However, as we will see below, the isotope mode calculation requires knowledge of the fully normalized localized mode displacement patterns. Following a procedure used by Page[9] in a different context, we can reexpress the normalization condition $\tilde{\chi}(f)[M_0+\Delta M]\chi(f)=1$ entirely in terms of defect-space quantities:

$$\tilde{\chi}_I(f)\left[\Delta M_{II}+C_{II}(\omega_f^2)\frac{dG_{0II}(\omega^2)}{d\omega^2}\Big|_{\omega=\omega_f}C_{II}(\omega_f^2)\right]\chi_I(f)=1. \tag{6}$$

This equation is derived by combining Eq. (2) with the normalization condition, using the identity $G_0(\omega^2)M_0G_0(\omega^2)=dG_0(\omega^2)/d\omega^2$, which follows from $(\Phi_0-\omega^2M_0)G_0(\omega^2)=I$, and using the localization property of ΔM and $C(\omega^2)$. Equation (6) allows the normalization constant to be computed readily, using just defect-space quantities.

The problem can be simplified even further by expanding C and G_0 in terms of a complete orthonormal set of symmetry basis vectors. This yields

$$C=\sum_{ip,tt'}C_B(\Gamma_i,tt')\xi(\Gamma_i p,t)\tilde{\xi}(\Gamma_i p,t')\ , \tag{7}$$

where Γ_i denotes an irreducible representation belonging to the point-symmetry group of the defect crystal, p labels the partners (rows) within the representation, and t labels the independent vectors for a given $\Gamma_i p$. The matrix elements of C in the symmetry basis are given by

$$C_B(\Gamma_i,tt')=\tilde{\xi}(\Gamma_i p,t)C\xi(\Gamma_i p,t')\ , \tag{8}$$

and they are independent of the partners. Similar expressions hold for G_0. This expansion follows from standard group-theory matrix element theorems, and it block diagonalizes the expressions for the local mode into blocks corresponding to each partner for each of the irreducible representations present in the defect space.

B. Infrared absorption

In the long-wavelength limit, the interaction between an insulator obeying the Born-Oppenheimer approximation and an external field of monochromatic infrared radiation is

$$\mathbf{M}(\mathbf{u})\cdot\mathbf{E}e^{-i\omega t}\ , \tag{9}$$

where $\mathbf{M}(\mathbf{u})$ is the system's dipole moment for nuclear configuration $\mathbf{u}$. Expanding the αth component of the dipole moment in terms of the nuclear displacements yields

$$\mathbf{M}^{\alpha}(\mathbf{u})=\sum_{l\beta}\mathcal{M}^{\alpha}_{\beta}(l)u_{\beta}(l)+\frac{1}{2}\sum_{l\beta,l'\beta'}\mathcal{M}^{\alpha}_{\beta\beta'}(l,l')u_{\beta}(l)u_{\beta'}(l')+\cdots , \quad (10)$$

where we have assumed a zero net dipole moment for the equilibrium configuration $\mathbf{u}=\mathbf{0}$. The linear term in this expansion is just a sum over the ionic displacements, multiplied by a set of effective charges $\boldsymbol{\mathcal{M}}^{\alpha}\equiv\{\mathcal{M}^{\alpha}_{\beta}(l)\}$. If we retain just the linear term and perform a calculation similar to one carried out by Klein,[10] the resulting absorption coefficient $\alpha(\omega)$ for a cubic crystal with an impurity concentration C_i is given by

$$\alpha(\omega)=\frac{4\pi\omega C_i}{cn(\omega)}\left[\frac{n_{\infty}^2+2}{3}\right]^2\tilde{\boldsymbol{\mathcal{M}}}^{\alpha}\,\mathrm{Im}[G(\omega^2+i\epsilon)]\boldsymbol{\mathcal{M}}^{\alpha} , \quad (11)$$

where $n_{\infty}=\sqrt{\epsilon_{\infty}}$ is the high-frequency index of refraction, c is the speed of light in vacuum, $G(\omega^2)=(\Phi-\omega^2 M)^{-1}$ is the harmonic Green's-function matrix for the *impurity* crystal and the limit $\epsilon\rightarrow 0^{+}$ is understood. In deriving this expression, we have assumed that the standard Lorentz local-field correction holds and that the contribution from the electronic polarizability is adequately described by the high-frequency dielectric constant ϵ_{∞}. The index of refraction $n(\omega)$ is taken to have its pure crystal value, owing to our assumption of low defect concentrations.

The Green's-function matrix can be written identically as a sum over the defect-crystal normal modes:

$$G(\omega^2)=\sum_{f}\boldsymbol{\chi}(f)\tilde{\boldsymbol{\chi}}(f)(\omega_f^2-\omega^2)^{-1} , \quad (12)$$

as is easily verified using Eq. (1) and the completeness relation $\sum_f M\boldsymbol{\chi}(f)\tilde{\boldsymbol{\chi}}(f)=I$. With $\omega^2\rightarrow\omega^2+i\epsilon$, we have $\mathrm{Im}G(\omega^2)=\pi\sum_f\boldsymbol{\chi}(f)\tilde{\boldsymbol{\chi}}(f)\delta(\omega_f^2-\omega^2)$, and the absorption constant becomes

$$\alpha(\omega)=\frac{4\pi^2\omega C_i}{cn(\omega)}\left[\frac{n_{\infty}^2+2}{3}\right]^2\times\sum_{f}\tilde{\boldsymbol{\mathcal{M}}}^{\alpha}\boldsymbol{\chi}(f)\tilde{\boldsymbol{\chi}}(f)\boldsymbol{\mathcal{M}}^{\alpha}\delta(\omega_f^2-\omega^2) . \quad (13)$$

Hence, the integrated absorption strength $S_f=\int\alpha(\omega)d\omega$ for a single local mode f is

$$S_f=\frac{2\pi^2 C_i}{cn(\omega)}\left[\frac{n_{\infty}^2+2}{3}\right]^2[\tilde{\boldsymbol{\mathcal{M}}}^{\alpha}\boldsymbol{\chi}(f)]^2 . \quad (14)$$

Using the transformation properties of the dipole moment, it is straightforward to show that for an impurity crystal with O_h symmetry, $\boldsymbol{\mathcal{M}}^{\alpha}$ transforms under symmetry operations as the αth partner of irreducible representation T_{1u}. Hence, by a standard group-theoretic matrix-element theorem, $\tilde{\boldsymbol{\mathcal{M}}}^{\alpha}\boldsymbol{\chi}(f)$ vanishes when $\boldsymbol{\chi}(f)$ is not an αth partner belonging to T_{1u}.

In Eq. (14), the sum $\tilde{\boldsymbol{\mathcal{M}}}^{\alpha}\boldsymbol{\chi}(f)=\sum_{l\beta}\mathcal{M}^{\alpha}_{\beta}(l)\chi_{\beta}(l|f)$ extends over the entire system, reflecting the fact that infrared radiation couples to all of the ions. For the case when the effective charges in the defect crystal are unperturbed from their host-crystal values, Klein[10] has shown how the absorption may be expressed in terms of just defect-space quantities. However, it will be shown in Sec. II D 1 below that the *relative* IR strengths of the pocket gap modes under isotopic host-lattice changes may be computed *without* the need to reduce Eq. (14) to defect-space quantities.

C. Impurity-model calculations

The determination of the local-mode displacement pattern and frequency requires knowledge of the pure crystal Green's-function elements. We employed two different methods to obtain these in the present study. The first is detailed in Refs. 9 and 11, and we now briefly summarize its present application. The breathing-shell model[12] was used to compute the pure KI phonon frequencies $\{\omega_{\mathbf{k}j}\}$ and complex plane wave displacement patterns $\{\boldsymbol{\chi}(\mathbf{k}j)\}$ at 22 932 $\mathbf{k}$ vectors in the irreducible $\frac{1}{48}$ element of the Brillouin zone, this being equivalent to one million vectors in the full zone. The imaginary parts of the unperturbed Green's-function matrix

$$\mathrm{Im}G_0(\omega^2)=\pi\sum_{\mathbf{k}j}\boldsymbol{\chi}(\mathbf{k}j)\boldsymbol{\chi}^{\dagger}(\mathbf{k}j)\delta(\omega_{\mathbf{k}j}^2-\omega^2)$$

were approximated as histograms by dividing the pure KI-phonon frequency range into 100 equally spaced bins and evaluating the sum $\sum'_{\mathbf{k}j}\boldsymbol{\chi}(\mathbf{k}j)\boldsymbol{\chi}^{\dagger}(\mathbf{k}j)$ over the modes whose frequencies fall within each bin. The real parts were then obtained by computing the Hilbert transforms of the imaginary parts.

Knowledge of the real and imaginary parts of the Green's-function matrix allowed us to compute the perturbed-band-mode properties (e.g., the resonant-mode absorption) as well as those for localized modes. However, for the case of localized modes, whose frequencies are necessarily outside the host-crystal phonon bands, the imaginary parts vanish, and it is only the real parts and their derivatives [needed for Eq. (6)] which were used for our gap-mode calculations. The derivatives were computed using numerical differentiation.

As a check on the preceding procedure, the real parts of the unperturbed Green's-function elements and their derivatives for frequencies outside the host-crystal phonon bands can also be determined by *direct* summation, using the formulas $G_0(\omega^2)=\sum_{\mathbf{k}j}\boldsymbol{\chi}(\mathbf{k}j)\boldsymbol{\chi}^{\dagger}(\mathbf{k}j)/(\omega_{\mathbf{k}j}^2-\omega^2)$ and $dG_0/d\omega^2=\sum_{\mathbf{k}j}\boldsymbol{\chi}(\mathbf{k}j)\boldsymbol{\chi}^{\dagger}(\mathbf{k}j)/(\omega_{\mathbf{k}j}^2-\omega^2)^2$. The T_{1u} 86.2-cm^{-1} gap-mode normalized displacement patterns calculated using this direct method differed by less than 3% from those calculated using the Hilbert transform method.

Our defect model for the low-temperature on-center configuration of KI:Ag^{+} consists of the mass change Δm, longitudinal force-constant changes $\delta\equiv-\Delta\Phi_{xx}(000,100)$ between the defect and each of its six nearest neighbors, and longitudinal force-constant changes $\delta'\equiv-\Delta\Phi_{xx}(100,200)$ between the defect's nearest-neighbor and adjacent fourth-nearest neighbors. Physically, δ arises from the different binding of the impurity

and is expected to be negative, consistent with the overall force-constant softening implied by the presence of the strong low-frequency IR impurity resonance at 17.3 cm^{-1}. The force-constant change δ' is postulated to arise from the expected defect-induced inward static relaxation of the nearest neighbors, also consistent with the overall force-constant softening.

Within this model, only the modes belonging to the T_{1u}, E_g, and A_{1g} irreducible representations of the O_h point group are perturbed. The necessary orthonormal symmetry basis vectors within the impurity space are shown in Fig. 2. The impurity space C matrices within these bases are given by

$$C_B(T_{1u})=\begin{bmatrix} 2\delta-\omega^2\Delta m & -\sqrt{2}\delta & 0 \\ -\sqrt{2}\delta & \delta+\delta' & -\delta' \\ 0 & -\delta' & \delta' \end{bmatrix} \tag{15}$$

and

$$C_B(A_{1g})=C_B(E_g)=\begin{bmatrix} \delta+\delta' & -\delta' \\ -\delta' & \delta' \end{bmatrix} . \tag{16}$$

The elements of the corresponding Green's-function matrices in these symmetry bases are listed in Table I.

The two force-constant changes (δ,δ') were determined by requiring that the model reproduce the observed T_{1u} 17.3-cm^{-1} low-frequency resonant and 86.2-cm^{-1} gap-mode IR frequencies.[7] *Both* the resonant- and gap-mode frequencies are determined by the condition $\mathrm{Re}|I+G_0(z)C(z)|=0$,[3] where $z=\omega^2+i\epsilon$. For the gap mode, the Re in this equation is of course superfluous. Using this condition, we computed δ' vs δ curves consistent with the 17.3- and 86.2-cm^{-1} T_{1u} modes, with the results given in Fig. 3. The crossing point of these two curves, denoted by a circle in the figure, gives the force-constant changes for which our model reproduces both of these T_{1u} absorption peaks. The corresponding fractional force-constant changes are $\delta/k_l=-0.563$ and $\delta'/k_l=-0.531$, where $k_l=1.884\times10^4$ dyn/cm is the pure KI breathing-shell-model nearest-neighbor longitudinal overlap force constant.

Having fixed the model's parameters, we next turn to its predictions. First, the model predicts the ratio of the IR absorption strengths for the 86.2- and 17.3-cm^{-1} gap and resonant modes to be 1.4.[7] This is in reasonable agreement with the observed value of ~3, considering that no local-field or effective charge changes were included in the relative intensity calculation. Second, the model predicts a low-frequency E_g resonance at 20.5 cm^{-1}, in good agreement with the observed E_g Raman

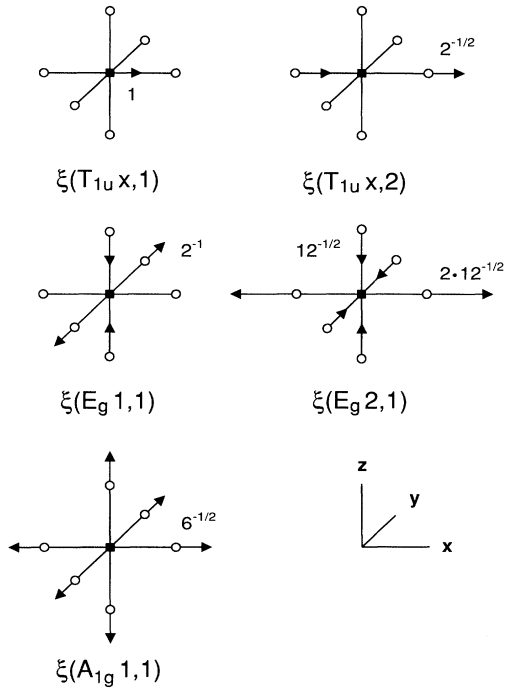

FIG. 2. Symmetry-basis vectors on the defect and its nearest neighbors, used in the perturbed phonon model. For a basis vector $\xi(\Gamma_i p,t)$, Γ_i labels the irreducible representation, p labels the partners (rows) within the representation, and t labels independent vectors for a given $\Gamma_i p$. For clarity, both partners are shown for the irreducible representation E_g. The impurity space for the perturbed phonon model also includes the defect's fourth-nearest neighbors [(±200), etc.], and the corresponding symmetry basis vectors [$\xi(T_{1u}x,3)$, $\xi(E_g1,2)$, $\xi(E_g2,2)$, and $\xi(A_{1g}1,2)$] for these sites are the same as those shown here for the first neighbors.

TABLE I. Green's-function elements needed for the impurity space, expressed in the symmetry basis discussed in the text and shown on the defect and its six nearest neighbors in Fig. 2.

$G_B(T_{1u},11)$	=	$G_{xx}(000,000)$
$G_B(T_{1u},12)$	=	$\sqrt{2}G_{xx}(000,100)$
$G_B(T_{1u},13)$	=	$\sqrt{2}G_{xx}(000,200)$
$G_B(T_{1u},22)$	=	$G_{xx}(100,100)+G_{xx}(100,-100)$
$G_B(T_{1u},23)$	=	$G_{xx}(100,200)+G_{xx}(100,-200)$
$G_B(T_{1u},33)$	=	$G_{xx}(200,200)+G_{xx}(200,-200)$
$G_B(A_{1g},11)$	=	$G_{xx}(100,100)-G_{xx}(100,-100)+4G_{xy}(100,010)$
$G_B(A_{1g},12)$	=	$G_{xx}(100,200)-G_{xx}(100,-200)+4G_{xy}(100,020)$
$G_B(A_{1g},22)$	=	$G_{xx}(200,200)-G_{xx}(200,-200)+4G_{xy}(200,020)$
$G_B(E_g,11)$	=	$G_{xx}(100,100)-G_{xx}(100,-100)-2G_{xy}(100,010)$
$G_B(E_g,12)$	=	$G_{xx}(100,200)-G_{xx}(100,-200)-2G_{xy}(100,020)$
$G_B(E_g,22)$	=	$G_{xx}(200,200)-G_{xx}(200,-200)-2G_{xy}(200,020)$

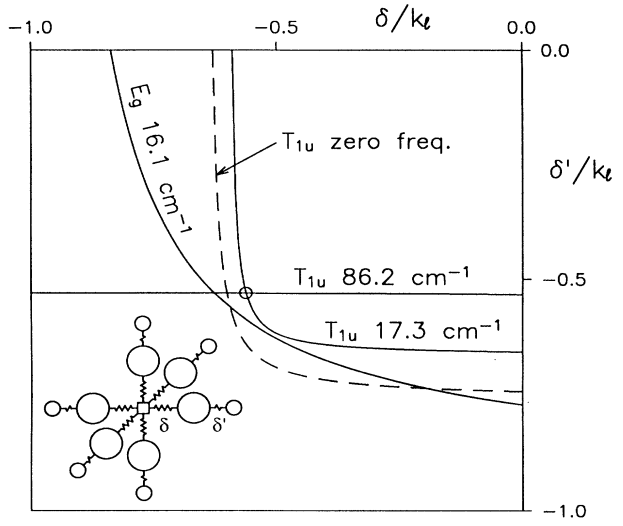

FIG. 3. Calculated fractional force-constant changes for resonant and gap modes at fixed frequencies. Inset: The force-constant perturbation in our model. The fractional changes are given in units of the pure breathing-shell-model nearest-neighbor longitudinal overlap force constant $k_l = 1.884 \times 10^4$ dyn/cm. The dashed curve corresponds to the onset of a T_{1u} instability. The fit values for the force-constant changes are $\delta/k_l = -0.563$, $\delta'/k_l = -0.531$. See Ref. 7.

peak at 16.1 cm^{-1}.[7,8] Figure 3 includes the δ' vs δ curve computed for an E_g resonance at 16.1 cm^{-1}, and one sees that this curve comes quite close to the circled (δ',δ) point for our model. For comparison, Fig. 3 also includes the (δ',δ) curve computed for the case of a *zero*-frequency T_{1u} resonance (dashed curve). The force-constant changes on this curve correspond to the defect lattice being unstable against T_{1u} displacements. We have found that as the force constants are weakened, the resonant mode of T_{1u} symmetry is almost always the first to become unstable; hence only the portion of Fig. 3 to the upper right of the dashed curve is physically reasonable. The close proximity of our fit point to the dashed curve means that our model corresponds to a nearly unstable defect-host system. The results of our low-temperature fit are summarized in Table II. Besides the T_{1u} and E_g resonant modes, the model also predicts an A_{1g} resonance at 37.3 cm^{-1}. This mode is Raman allowed, but was not seen experimentally.[7] However, we note that the A_{1g} and E_g Raman strengths are determined by two independent electronic polarizability derivatives, so that the null A_{1g} experiment could be used to place bounds on these derivatives.

As discussed in the Introduction, the most striking prediction of our model is the existence of three nearly degenerate gap modes of A_{1g}, E_g, and T_{1u} symmetry. These modes have some very unusual properties. The first is the extent of the near degeneracy—the frequencies are within about a wave number of each other. Second, they are essentially independent of the force-constant change δ, as is evident from the curve for the 86.2-cm^{-1} gap mode in Fig. 3. Third, ratios of the Raman strengths

TABLE II. Measured and calculated IR and Raman frequencies (in cm^{-1}) for KI:Ag^+. The defect-model harmonic force-constant changes δ and δ' were fit to the measured T_{1u} resonant- and gap-mode frequencies, as indicated. The predicted ratio between the T_{1u} resonant- and gap-mode absorption strengths is $S(86.2)/S(17.3) = 1.4$, and the experimental value is ~3. See Ref. 7.

Mode symmetry	Observed	Calculated
T_{1u}	17.3	17.3 (fit)
T_{1u}	86.2	86.2 (fit)
E_g	16.1	20.5
A_{1g}	Unobserved (see text)	37.3

of the A_{1g} and E_g gap modes to their low-frequency resonant-mode counterparts are predicted to be negligible. Indeed, these modes were not observed in Raman experiments.[7]

Detailed calculations of the mode displacement patterns reveal the origin of these unusual properties. All three gap modes have displacements patterns which are strongly peaked on the impurity's fourth-neighbor sites $[(\pm 200),(0\pm 20),(00\pm 2)]$, as shown in Fig. 1. The displacements on these sites are a factor of 50 or more larger than those on the impurity or its six nearest neighbors. The nearly degenerate frequencies of these "pocket" modes reflect the fact that they are almost entirely determined by the local dynamics within each pocket; the pockets are weakly coupled to produce the different symmetry modes. Moreover, the independence of these modes on the force-constant change δ is clear, since this force-constant change couples ions which have essentially no motion in these modes. Finally, the weak predicted Raman strengths for the A_{1g} and E_g pocket modes is also explained by the negligible displacements on the impurity's nearest neighbors, since defect-induced first-order Raman scattering in alkali halides typically arises from the modulation of the electronic polarizability by the motion of the ions in the impurity's immediate vicinity. On the other hand, the T_{1u} pocket mode is readily observable with IR absorption, since this probe couples to *all* of the ions in the system. Unfortunately, our model is fit to the measured IR pocket-mode frequency, so that the negligible Raman activity of the two even-parity pocket modes precludes a straightforward independent verification of the existence of these highly unusual modes.

D. Isotope mode splitting

1. Theory

Owing to the negligible Raman activity of the A_{1g} and E_g pocket gap modes, we need another test to verify their existence. Fortunately, the naturally occurring isotopic abundances of 7% $^{41}K^+$ and 93% $^{39}K^+$ in the host crystal provide just such a test. We will now show that our harmonic-defect model predicts that the presence of one or more $^{41}K^+$ ions at the impurity's fourth-neighbor sites strongly mixes the pocket gap modes of all three symme-

try types, producing new IR-active "isotope" pocket gap modes which should be experimentally observable.

To determine the frequencies and IR-integrated absorption strengths for these isotope modes, we first apply nearly degenerate perturbation theory to a single impurity-isotope combination. This is done by expanding the isotope-mode displacement patterns in terms of the six normalized unperturbed pocket-gap-mode patterns $\psi(i)=\sum_{f'=1}^{6}a_{f'}(i)\chi(f')$ and substituting the expansion into Eq. (1). Here $i=1,\ldots,6$ labels the isotope modes. Multiplying the resulting equation on the left by $\tilde{\chi}(f)$ yields a 6×6 eigenvalue equation for the isotope-mode frequencies ω_i and the expansion coefficients $a_f(i)$:

$$(\omega_{0f}^2-\omega_i^2)a_f(i)=\sum_{f'=1}^{6}\omega_i^2\tilde{\chi}(f)\Delta m\chi(f')a_{f'}(i)\ . \qquad (17)$$

Here Δm is the diagonal matrix containing the mass changes introduced by the $^{41}K^+$ isotopes, and the $\{\omega_{0f}\}$ are the six unperturbed pocket-gap-mode frequencies. The $\{\psi(i)\}$ are *zeroth-order* displacements, and the normalization condition $\tilde{\psi}(i)M\psi(i)=1$ implies that $\sum_{f=1}^{6}a_f^2(i)=1$. With the transformation $b_f(i)=a_f(i)\omega_{0f}$, we can rewrite Eq. (17) in the standard eigenvalue form:

$$(\omega_0^{-1}A\omega_0^{-1}-\omega_i^{-2}I)\mathbf{b}(i)=0\ , \qquad (18)$$

where $A_{ff'}=\delta_{ff'}+\tilde{\chi}(f)\Delta m\chi(f')$, and ω_0 is a diagonal matrix formed from the unperturbed gap-mode frequencies.

A ^{41}K isotope substitution changes the mass of the K^+ ion, leaving its electronic structure and, hence the effective charges $\mathcal{M}^\alpha$ introduced in Eq. (10) unchanged. Thus the dipole moments for the isotope modes are produced exclusively by their T_{1u} components. With this in mind, we substitute $\psi(i)$ into Eq. (14) and find that the integrated x-polarized IR absorption for the ith isotope mode, of frequency ω_i and produced by a *single* impurity-isotope combination in a crystal of volume V, is given by

$$s_i=\frac{2\pi^2}{cn(\omega_i)V}\left[\frac{n_\infty^2+2}{3}\right]^2[\tilde{\mathcal{M}}^x\chi(T_{1u}x)]^2a_{T_{1u}x}^2(i)\ . \qquad (19)$$

This expression is just the absorption for a single impurity with no isotopes present, multiplied by the $T_{1u}x$ fraction $a_{T_{1u}x}^2(i)$ for the ith isotope mode and by an index of refraction correction $n(\omega_{T_{1u}})/n(\omega_i)$.

2. Numerical results

Figure 4 shows our calculated splittings for a single Ag^+ impurity with a (200) $^{41}K^+$ isotopic substitution, which mixes the A_{1g}, E_g2, and T_{1u} x pocket gap modes to create three isotope modes. The calculated displacement patterns for the (200) isotope modes with the largest and smallest frequency shifts from the unperturbed T_{1u} 86.2-cm^{-1} pocket gap mode are found to be confined to a single pocket. The pattern for the isotope mode at 84.7 cm^{-1} is strongly peaked on the (200) site, whereas that for the 86.1-cm^{-1} isotope mode is strongly peaked at (-200).

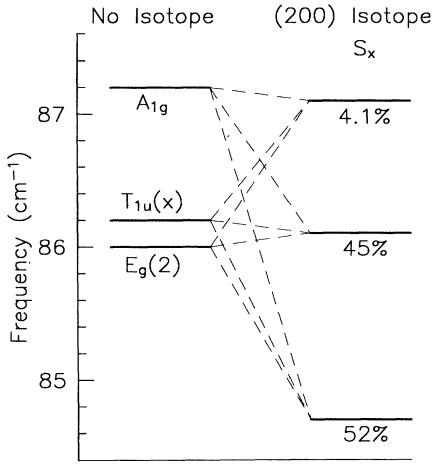

FIG. 4. Mixing of the three nearly degenerate A_{1g}, E_g2, and $T_{1u}x$ gap modes under a (200) $^{39}K^+\rightarrow{}^{41}K^+$ host-lattice isotopic substitution. The percentages give the strength s_x of the x-polarized absorption per defect/(200) isotope combination relative to a defect with no isotope substitution. Note that the percentages add up to slightly more than 100% because the absorption coefficient is not only proportional to the imaginary part of the dielectric function but is also inversely proportional to the host-crystal index of refraction, which is strongly frequency dependent in the gap-mode region. See Ref. 4.

As shown in Fig. 4, fourth-neighbor $^{41}K^+$ substitutions can produce isotope modes having frequency shifts larger than 1 cm^{-1} and IR-absorption strengths comparable to that produced by a defect with no isotopes present. In contrast, we find that (110) (i.e., second-neighbor) and (400) $^{41}K^+$ isotope substitutions produce modes have negligible absorption strengths and/or frequency shifts of less than 0.1 cm^{-1}, which, given the large width of the main mode, would be very difficult to observe. If we were to include the weakly shifted but relatively strong modes produced by these isotopes in our calculations, the resulting unperturbed mode strength would be less than if these modes were neglected. But in order to compare theory and experiment, the strengths of these weakly shifted modes would have to be added to the unperturbed mode strength. Furthermore, since the displacements for the isotope mode are zeroth-order displacements in our perturbation approach, the $T_{1u}x$ fractions $a_{T_{1u}x}^2(i)$ for a single isotope-impurity combination sum to unity. Hence, one sees from Eq. (19) that, provided we can neglect the change with frequency of the index of refraction, which is an excellent approximation for modes separated by less than 0.1 cm^{-1}, the unperturbed mode strength obtained by including the weakly shifted modes is the same as if their contributions had been neglected from the outset. Similar arguments hold for the splitting of the pocket isotope modes, such as the 84.7-cm^{-1} (200) $^{41}K^+$ mode, due to second-neighbor or (400) $^{41}K^+$ isotopes—as long as the splitting produced by these substitutions is smaller than the experimental resolution, or these new modes have negligible absorption strengths compared with the fourth-neighbor pocket isotope

modes, their contributions can be ignored. Accordingly, the second-neighbor and (400) $^{41}K^+$ isotope substitutions will be neglected in our isotope-induced IR-absorption calculations. However, in order to account for all $^{41}K^+$ *fourth*-neighbor modes, we will include $^{41}K^+$ fourth-neighbor isotope modes with frequency shifts of less than 0.1 cm^{-1}.

Our nearly degenerate perturbation theory predicts the frequency shifts and integrated IR-absorption strengths for isotope modes produced by a *single* impurity-isotope combination. However, in a real KI:Ag^+ system, there is a distribution of impurity-isotope combinations. Hence, in order to predict the experimental strengths, we need to multiply our computed strengths for single impurity-isotope combinations by the average number of times these combinations occur.

The probability that a single impurity will have l $^{41}K^+$ isotopes as fourth neighbors is

$$p(l)=\frac{6!}{l!(6-l)!}(1-f)^{6-l}f^l , \tag{20}$$

where f is the fraction of the K^+ ions which are $^{41}K^+$ isotopes. For $f=0.07$, we have $p(0)=0.647$, $p(1)=0.292$, $p(2)=0.055$, and $p(3)=0.0055$. Since impurities with three or more $^{41}K^+$ ions as fourth neighbors account for less than 1% of the impurities in a sample, we neglect these impurity-isotope combinations in our calculations. This leaves 22 unique impurity-isotope combinations to consider. However, symmetry further reduces the number of impurity-isotope combinations that produce isotope modes with unique frequencies and x-polarized strengths to six, namely: (200), (020), (200)-(-200), (200)-(020), (020)-(0-20), and (020)-(002). For example, the seven $^{41}K^+$ (200)-(0-20), (-200)-(020), (-200)-(0-20) and ($\pm$200)-(00$\pm$2) $^{41}K^+$ isotope substitutions each produce five x-polarized IR-active modes, having the same set of frequencies and absorption strengths as those produced by a (200)-(020) $^{41}K^+$ substitution.

In a crystal with N_d impurities, the predicted x-polarized strength for the ith isotope mode produced by an impurity-isotope combination with l fourth-neighbor isotopes plus the N_i-1 equivalent modes produced by different isotope-impurity combinations, also with l $^{41}K^+$ fourth neighbors, is given by

$$S_i=N_dN_i(1-f)^{6-l}f^l s_i , \tag{21}$$

where s_i is the x-polarized strength for the ith mode produced by a *single* isotope-impurity combination, as given by Eq. (19). Table III lists the frequencies, "degeneracy factors" N_i and relative x-polarized absorption strengths S_i produced by the six unique impurity-isotope combinations chosen above.

There are thirteen modes listed in Table III. To compare our predicted isotope-mode spectrum with the experimentally observed spectrum, we combine modes within $\sim$0.2 cm^{-1} of each other, expecting that they will not be observable. This gives two predicted isotope "modes" which can be resolved from each other and from the main line. Accordingly, we take the strength-weighted average frequency $\bar{\omega}\equiv\sum_i S_i\omega_i/\sum_i S_i$ as the frequency of each of these two combined modes. Here the sum runs over just the modes which are being combined. As one can see from Table III, the two isotope modes produced by a (200) isotope combination that are resolvable from the no-isotope mode will dominate these combined modes. Of the thirteen modes in Table III, four (lines 2, 6, 9, and 12) contribute to the lower-frequency combined mode, two (lines 4 and 11) contribute to the higher-frequency combined mode, and the remaining seven contribute to the main line. Finally, since we are going to compare *relative* absorption intensities between these modes and the main T_{1u} gap mode at 86.2 cm^{-1},[13] the expressions for the intensities will only involve the index of refraction and the T_{1u} mode fraction factors; taking the ratio eliminates the effective charges present in Eq. (19).

TABLE III. Impurity-isotope combinations which produce modes with unique frequencies and x-polarized absorption strengths. N_i is the degeneracy factor explained in the text. The x-polarized absorption strengths S_i are normalized with respect to the strength for the mode with no isotopes present and include the contributions from impurity-isotope combinations that produce isotope modes with the same frequency and x-polarization strengths as the modes listed in the table. Before comparing these predictions with experiment, the modes which cannot be resolved experimentally need to be combined, as discussed in the text.

$^{41}K^+$ sites	ω_i (cm^{-1})	N_i	S_i/S_0
–	86.2	1	1.00
(200)	84.7	2	0.078
(200)	86.1	2	0.068
(200)	87.1	2	0.0062
(020)	86.2	4	0.30
(200)-(-200)	84.6	1	0.0058
(020)-(0-20)	86.2	2	0.057
(020)-(002)	86.2	4	0.023
(200)-(020)	84.9	8	0.014
(200)-(020)	86.1	8	0.0065
(200)-(020)	87.0	8	0.0024
(200)-(020)	84.6	8	0.010
(200)-(020)	86.1	8	0.013

The predicted frequency shifts and relative strengths for the two isotope modes expected to be experimentally resolvable are listed in Table IV, together with the experimental observations. The predicted and experimental results for the lower-frequency isotope mode are seen to be in good agreement, especially considering that there were no adjustable parameters. The higher-frequency mode at 87.1 cm^{-1} is presumably too weak to be observed. Further discussion of these results will be deferred until after the following section, which details the experiments.

III. EXPERIMENT

A. Observation of the isotope mode

The samples were cleaved from crystals of KI:Ag^+ grown by the Czochralski method at the Cornell Materials Science Center Crystal Growing Facility. Care was

TABLE IV. Calculated and measured pocket-gap-mode isotope splittings and strengths for KI:Ag^+ due to the 7% abundance of $^{41}K^+$ in the host crystal, relative to the "unperturbed" gap mode at 86.2 cm^{-1}. The unperturbed gap-mode strength used to calculate the observed relative absorption strengths includes contributions from isotope modes unresolvable from the 86.2-cm^{-1} mode, as discussed in the text. The mode at 87.1 cm^{-1} is too weak to be observed.

	Calculated	Observed	Calculated	Observed
Frequency (cm^{-1})	84.7	84.5	87.1	–
Frequency splitting (cm^{-1})	−1.5	−1.7	0.9	–
Relative strength	0.07	0.04	0.006	–

taken to choose the pure KI starting material from which the crystals were grown in order to minimize the presence of impurities that give rise to far-infrared modes with frequencies near those caused by the Ag^+ dopant. A variable-temperature optical-access cryostat was used to cool the samples to superfluid-helium temperatures; for the temperature-dependent studies, the samples were immersed in either helium liquid or gas. A rapid-scanning Fourier-transform interferometer was used to accumulate high-resolution (0.1 cm^{-1}) spectra with good signal-to-noise ratios between 69 and 96 cm^{-1}, the phonon gap region of KI. Further details of the experimental techniques for such measurements are given in Ref. 14.

1. Absorption spectrum

The absorption coefficient of KI+0.4 mol% AgI in the phonon gap region of KI for two different temperatures is shown in Fig. 5 at a resolution of 0.1 cm^{-1}. The strong impurity-induced feature at 86.2 cm^{-1} is the KI:Ag^+ gap mode corresponding to the low-temperature on-center configuration of the defect system. Most of the weaker spectral features seen here and identified in the figure caption are associated with other unwanted monatomic impurities, present in either the host or dopant starting materials. When the temperature is increased from 1.6 to 8.8 K, the strengths of this strong Ag^+ gap mode and a neighboring satellite line at lower frequency are reduced by a factor of 2, while the strengths of the weak but sharp modes due to the other impurities remain unchanged. The center frequencies of these two Ag^+ modes show a very small shift to lower frequencies with increasing temperature, which cannot be seen in this figure. At the highest frequencies shown in the figure, the temperature change produces an increase in the host absorption coefficient due to intrinsic difference-band processes.[15]

The interplay between the temperature dependence of the gap-mode strength and the underlying difference-band absorption can be more easily seen in the three-dimensional plot of Fig. 6, which displays the results obtained for a number of temperatures from 1.6 to 19 K. At the highest temperature shown, 19.0 K, the gap mode has nearly vanished; the remaining weak absorption peaks at 86.3 and 86.9 cm^{-1} are due to a small concentration of naturally occurring Rb^+ impurities.[14] It is clear from these data that not only does the strength of the main mode disappear with increasing temperature, but also that the weak satellite line at 84.5 cm^{-1} disappears with a similar temperature dependence. At the same time that the difference-band absorption increases in magnitude with increasing temperature, the weak features within and on the high-frequency side of the main Ag^+ gap mode remain essentially temperature in-

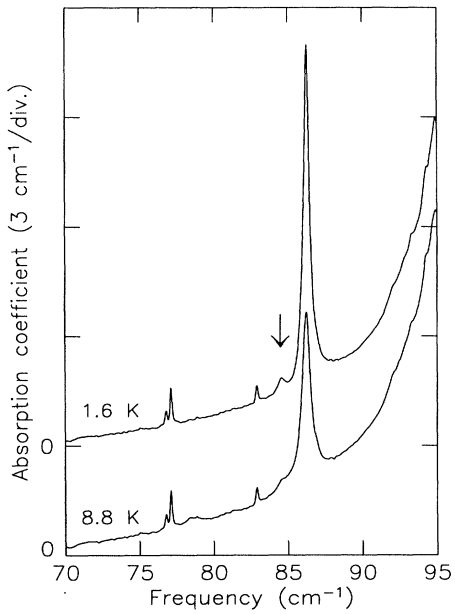

FIG. 5. Impurity-induced absorption coefficient of KI+0.4 mole% AgI. The restricted frequency interval covers the phonon gap region of KI. The resolution is 0.1 cm^{-1}. The temperature of the upper spectrum is 1.6 K, and that of the lower one is 8.8 K. The strong mode at 86.2 cm^{-1} is the on-center KI:Ag^+ gap mode. This mode has lost about half its strength in the higher-temperature spectrum. The doublet at 76.8 and 77.1 cm^{-1} is due to Cl^- and the single peak at 82.9 cm^{-1} is due to Cs^+. The weak temperature-dependent peak at 84.5 cm^{-1} is the Ag^+ isotope mode. Note that the KI:Ag^+ modes, which have a FWHM of ~0.5 cm^{-1}, are significantly broader than other KI gap modes, whose FWHM is ~0.14 cm^{-1}. Additional temperature-induced changes are increased broad-band absorption due to difference-band processes in the host KI crystal and the appearance of a KI:Ag^+ gap mode at 78.6 cm^{-1} corresponding to the population of another configuration of the Ag^+ defect in the KI lattice.

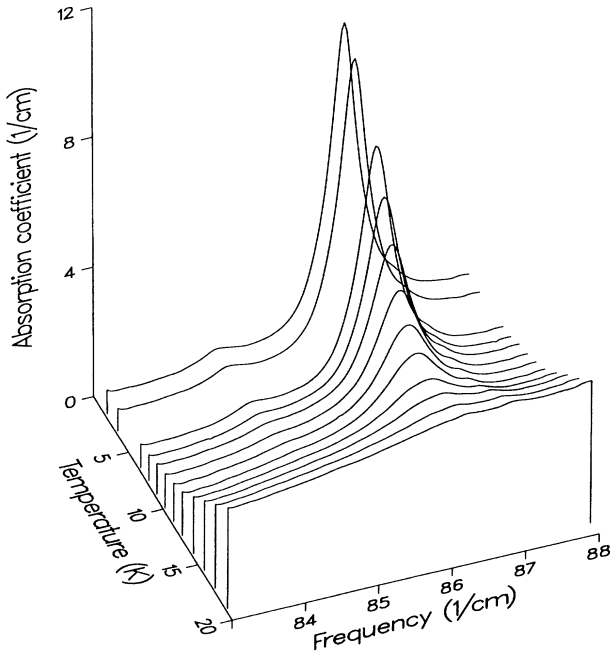

FIG. 6. Temperature dependence of the absorption coefficient in the region of the KI:Ag^+ pocket gap modes between 1.6 and 19 K. The samples are the same as in Fig. 5. The resolution is 0.1 cm^{-1}. Note that the two KI:Ag^+ modes have nearly disappeared in the high-temperature spectrum, where two weak Rb^+ gap modes at 86.3 and 86.9 cm^{-1} have become visible. Note also the dramatic increase in the difference-band absorption with increasing temperature.

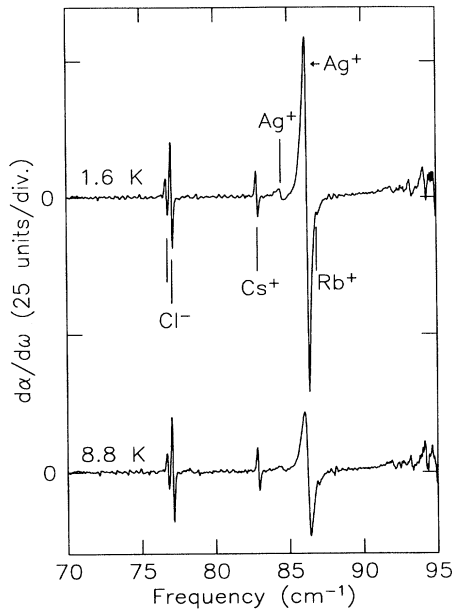

FIG. 7. Derivatives of the spectra in Fig. 5. This view brings out the weak Rb^+ mode at 86.9 cm^{-1} (the even weaker 86.3-cm^{-1} Rb^+ mode is nearly coincident with the much stronger 86.2-cm^{-1} Ag^+ mode, and is hidden at low temperatures). The main advantage of this representation is the suppression of the broad-band background.

dependent but become easier to see with the disappearance of the Ag^+ gap mode.

An identifiable property of the Ag^+ gap modes at 86.2 and 84.5 cm^{-1} is that their strengths become vanishingly small by $\sim$25 K.[4,5,16] This temperature dependence is associated with the depopulation of the Ag^+ on-center configuration[5] and is exhibited by all experimental probes of this defect system.[5–7] In contrast, the KI:Cl^- doublet at 76.8 and 77.1 cm^{-1} and the KI:Cs^+ single peak at 82.9 cm^{-1} in Fig. 5, for example, have no temperature dependence in this restricted temperature region.

There is another relevant feature generated by the Ag^+ defect in the 8.8-K spectrum of Fig. 5. A weak broad gap mode is visible at 78.6 cm^{-1}, which initially grows in strength with increasing temperature. Previously, this line was identified with a transition in the off-center Ag^+ configuration.[5] The more precise temperature-dependent data that we shall show in Sec. III A 3 indicate that this initial assignment is not correct.

In order to determine the Ag^+ concentration dependence of the weak satellite mode at 84.5 cm^{-1}, tentatively identified as an isotope pocket gap mode, we measured spectra of samples with nominal concentrations of 0.1 and 0.4 mole %. The peak absorption values for the strong 86.2-cm^{-1} pocket gap mode, which are proportional to the actual concentrations, were found to be 6.2 and 11.8 cm^{-1}, respectively, for the two boules (the actual concentrations are substantially lower than the nominal ones). In both cases, the isotope mode had a strength of 4% relative to that of the main mode, obtained by the fitting procedure described in Sec. III B 1 below, indicating that both modes depend linearly on the Ag^+ concentration. This test verifies that the weak satellite is not a pair-mode feature.

2. *Derivative of the absorption spectrum*

To search for the other weak isotope-shifted pocket modes predicted by the theory, we have analyzed the derivatives of the impurity-induced absorption spectra in addition to the spectra themselves. The derivatives of the spectra of Fig. 5 are shown in Fig. 7. Note that the temperature-dependent difference-frequency absorption background is suppressed by this manipulation of the data. The weak but sharp features identified in Fig. 5 are much easier to see in Fig. 7. For example, the weak temperature-independent KI:Rb^+ mode at 86.9 cm^{-1}, which is almost totally obscured by the nearby strong KI:Ag^+ pocket gap mode at 86.2 cm^{-1} in the low-temperature spectra of Figs. 5 and 6, is clearly seen in the derivatives in Fig. 7. The source of the additional absorption features which occur above 90 cm^{-1} have not yet been identified.

Figure 8 presents an expanded version of the derivatives in the Ag^+ gap-mode region. The two arrows mark the locations of the two pocket gap modes predicted by the model to result from the isotopic substitution and expected to be resolvable, as listed in Table IV. One obvi-

ous assignment is to identify the line at 84.5 cm^{-1} with the stronger of these predicted isotope modes at the slightly larger frequency of 84.7 cm^{-1}. The primary source of this mode is the mixing of the 86.2-cm^{-1} pocket gap mode with the even-parity pocket gap modes, due to the replacement of $^{39}K^+$ by $^{41}K^+$ (93% and 7% natural abundances, respectively) at the (±200) lattice sites relative to that occupied by the Ag^+ defect.

Another somewhat weaker feature is observed at 85.8 cm^{-1} in Fig. 8, on the wing of the main line at 86.2 cm^{-1}. Although Fig. 9 presents the derivative spectra for temperatures ranging from 1.6 to 19 K, it is difficult to conclude much about this weak satellite at 85.8 cm^{-1} from these data. Since the highest-temperature results do not show the shoulder observed in the low-temperature spectra, it is possible that this shoulder is associated with one of the weakly shifted $^{41}K^+$ isotope modes, such as the 86.1-cm^{-1} mode given in third line of Table III. However, because of the interference by the strong unperturbed mode at 86.2 cm^{-1}, it is not possible to make an unambiguous assignment.

The abscissa in the center part of Fig. 9 has been expanded 10× in order to demonstrate the qualitative similarity between the temperature dependence of the main pocket gap mode and that of the isotope pocket mode. For contrast, Fig. 9 also shows the 82.9-cm^{-1} KI:Cs^+ gap mode, whose strength has no temperature dependence in this restricted temperature range.

Similarly, the very weak high-frequency pocket isotope mode predicted by theory (see Fig. 8) is outside the absorption line shape produced by the main unperturbed line but is nearly on top of a Rb^+ gap mode. Inspection

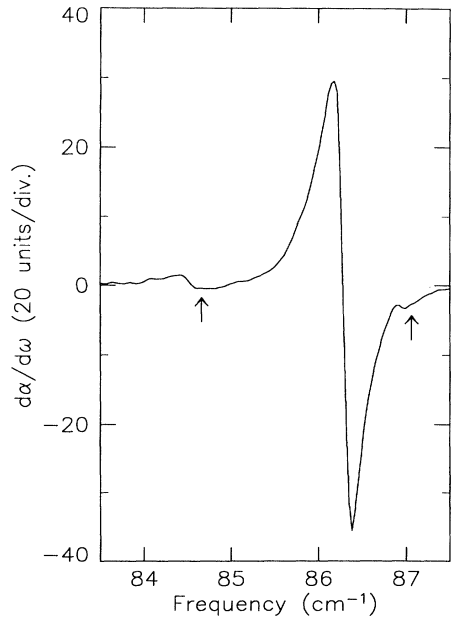

FIG. 8. Expanded view of the derivative of the low-temperature gap-mode spectrum. The arrows mark the positions of the two resolvable pocket modes predicted by the model in the presence of a (200) $^{39}K^+ \rightarrow {}^{41}K^+$ isotope substitution, as discussed in the text. The observed mode at 84.5 cm^{-1} is identified with the predicted mode at 84.7 cm^{-1}. The very weak shoulder at 85.8 cm^{-1} may correspond to the isotope mode predicted at 86.1 cm^{-1}, but the mode predicted at 87.1 cm^{-1} would be nearly coincident with the 86.9-cm^{-1} Rb^+ mode.

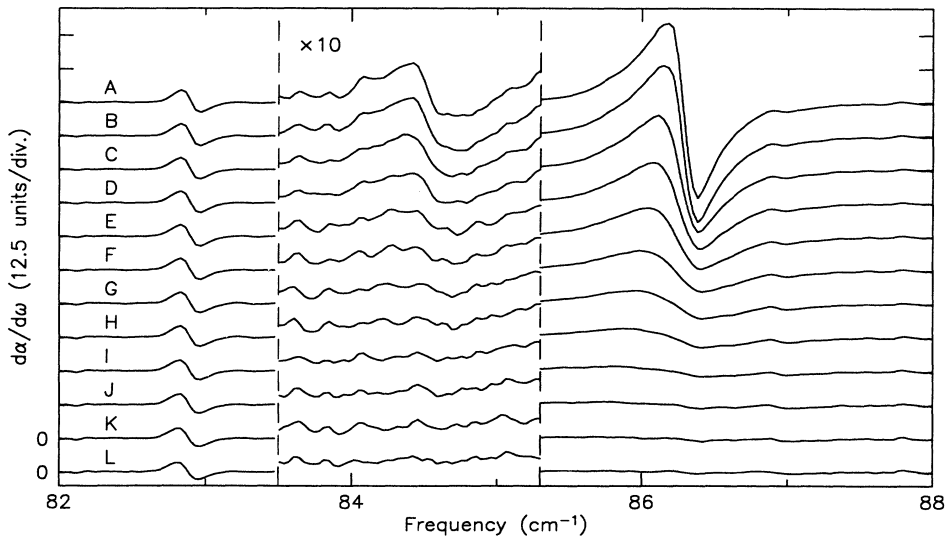

FIG. 9. Temperature dependence of the derivative of the absorption coefficient in the gap mode region. The temperatures range from 1.6 to 19.0 K. The abscissa in the center section is magnified ten times in order to show the KI:Ag^+ isotope mode more clearly. For contrast, the lowest-frequency section shows the nearly temperature-independent Cs^+ mode at 82.9 cm^{-1}. Note the qualitative similarity between the temperature dependences of the gap mode and the isotope mode. The temperatures of the spectra are: *A*, 1.6 K; *B*, 3.1 K; *C*, 6.4 K; *D*, 7.6 K; *E*, 8.8 K; *F*, 10.0 K; *G*, 11.2 K; *H*, 12.4 K; *I*, 14.0 K; *J*, 15.6 K; *K*, 17.2 K; *L*, 19.0 K.

of the derivative spectra in Fig. 9 does not give any additional evidence that a temperature-dependent feature occurs in this region. An assignment with the high-frequency mode in Table IV is therefore not possible.

3. *Absorption difference spectrum*

A different way of investigating the temperature dependence of the Ag^+ modes is by looking at the difference in absorption coefficient between a temperature T and the lowest measured temperature of 1.6 K. These results, presented in Fig. 10, bring out only the region of increased absorption at higher temperatures. To expand the ordinate scale, we have excluded the strong unperturbed KI:Ag^+ pocket gap mode in order to allow a closer look at the weaker modes. Trace *A* (a horizontal line) shows that there is no change in the absorption coefficient between 1.6 and 3.1 K. Trace *B* shows that an observable change is found at 6.4 K, and so on. Aside from the decrease in the strength of the isotope mode and the increase in the strength of the broad "off-center" KI:Ag^+ band at 78.6 cm^{-1} with increasing temperature, this view also reveals two unexpected results: (1) There is a narrow spectral region between the unperturbed and isotope KI:Ag^+ pocket gap modes, centered at ~85.3 cm^{-1}, where the absorption coefficient appears to increase faster with temperature than the intrinsic difference-band absorption. At higher temperature, the absorption coefficient in this region is controlled by the difference-band absorption; hence it is evident from Fig. 10 that this initial effect does not continue to grow. (2) The 78.6-cm^{-1} band grows with increasing temperature but then appears to stop changing for temperatures larger than about 12 K. It seems that the temperature dependence of the strength of this mode and the one at 85.3 cm^{-1} may be related. But, in any case, neither of these strengths show the temperature dependence associated with the off-center configuration[5,7] which continues to grow in strength until about 25 K. It is unexplained features such as these which make us cautious in assigning the 86.1-cm^{-1} isotope mode to the satellite at 85.8 cm^{-1}. We note that even though only one of the two resolvable isotope modes has been unambiguously identified experimentally (84.5 cm^{-1}), both the measured low-temperature center frequency and strength of this mode are consistent with the theoretical pocket-mode predictions summarized in Table IV.

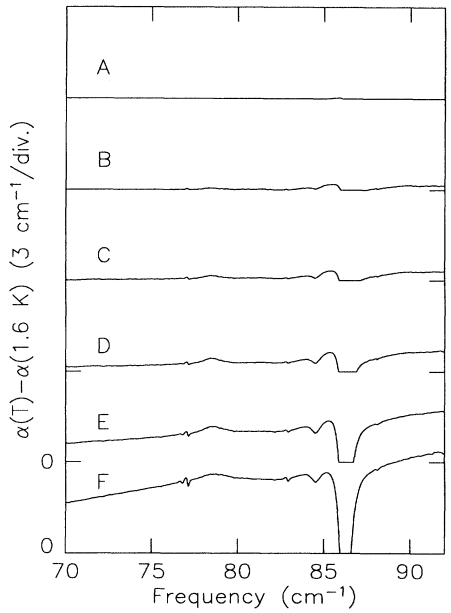

FIG. 10. Temperature dependence of the change in the absorption coefficient in the gap mode region. The reference temperature is 1.6 K. In order to magnify the ordinate, only the *increased* absorption range is shown in each trace. The strongly temperature-dependent KI:Ag^+ pocket gap modes are readily visible in the higher-temperature spectra. A region of increased absorption between these two Ag^+ gap modes appears at surprisingly low temperatures. The Cl^- and Cs^+ modes are suppressed here because they are nearly temperature independent. The higher-temperature spectra indicate the appearance of another KI:Ag^+ gap mode at 78.6 cm^{-1} on top of the rapidly increasing difference-band background. The temperatures (T) associated with the difference spectra are: *A*, 3.1 K; *B*, 6.4 K; *C*, 7.6 K; *D*, 10.0 K; *E*, 14.0 K; *F*, 19.0 K.

B. Temperature dependence of the gap-mode strength

1. *Difference-band background subtraction method*

In order to quantify the temperature dependences of the KI:Ag^+ pocket gap modes, it is necessary to separate the spectral lines from the intrinsic background absorption. This procedure is especially complicated in the case of the isotope mode because part of the background in its spectral region is due to the much stronger higher-frequency unperturbed Ag^+ pocket gap mode. The original method used for the unperturbed gap mode was to subtract a "reasonable" background and then numerically integrate the remaining peak;[5] the result is shown as the dashed line in Fig. 11(a). It was also found[7] that the strengths of other experimentally measured properties, such as the IR-active resonant mode at 17.3 cm^{-1}, the Raman-active resonant mode at 16.1 cm^{-1}, the UV transitions, and the ac dielectric susceptibility could be related to the same dashed line.

An improved technique, which we now describe, consists of a systematic fitting procedure from which the strengths of both the unperturbed and isotope gap modes can be obtained. First, the data in the parts of the phonon gap region of KI where no impurity modes are present is used to fit a ninth-order polynomial to the temperature-dependent background absorption. Second, the background absorption is subtracted, leaving only the absorption peaks corresponding to the impurity modes. Third, the strengths of the KI:Ag^+ pocket gap modes are obtained by fitting the peaks to the sum of two Voigt functions[17] (convolutions of a Gaussian and a Lorentzian function), corresponding to the unperturbed and isotope modes, respectively. Since the isotope mode is much weaker than the unperturbed mode (4% of the strength; see Table IV), it is necessary to limit the number of free

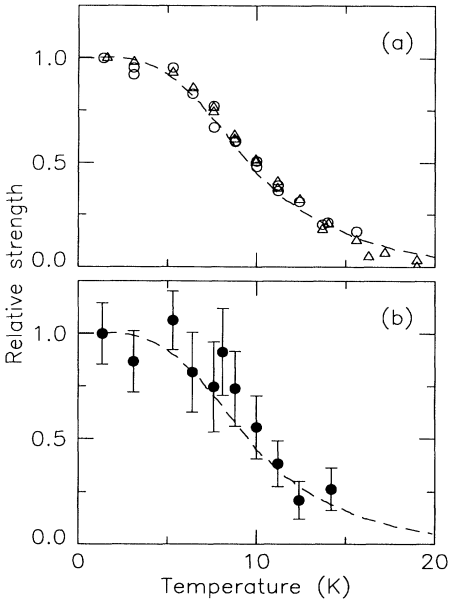

FIG. 11. Temperature dependences of the pocket-gap-mode strengths for KI:Ag^+. The dashed line in both parts of the figure is the previously measured temperature dependence of the gap and resonant modes, as well as of the UV electronic transitions, ac susceptibility, and a Raman-active mode associated with the on-center configuration of this defect system (Refs. 5–7). (a) Temperature dependence of the strength of the unperturbed KI:Ag^+ pocket gap mode at 86.2 cm^{-1}, as obtained by two different analytical techniques (symbols). Circles: strength obtained by fitting the absorption peak to a Voigt function following background subtraction. Triangles: strength obtained from the derivative of the spectrum, which obviates the need for background subtraction (see text). (b) Temperature dependence of the strength of the KI:Ag^+ isotope pocket gap mode at 84.5 cm^{-1} (symbols), as obtained by fitting to the sum of two Voigt functions following background subtraction (see text).

parameters in the fits: the assumptions used are that the two Voigt functions have the same shape and that the separation of their center frequencies is temperature independent. Thus the remaining free parameters are the widths of the Gaussian and Lorentzian contributions to the line shapes and the strengths of the two modes. In general, excellent fits are obtained, especially at the lower temperatures. The strength of the unperturbed gap mode obtained by this technique is shown as the circles in Fig. 11(a) and is in good agreement with the previous results, represented by the dashed line. Figure 11(b) shows the temperature dependence of the isotope mode as determined by this technique; within the experimental uncertainty, the temperature dependences of the unperturbed and isotope KI:Ag^+ pocket gap modes are clearly similar, and possibly identical.

2. *Derivative method*

A problem with the preceding fitting procedure is that the shape of the temperature-dependent background subtracted from the data systematically affects the temperature dependence of the strengths of the modes. To check this potential systematic error, we have developed a different way to determine the strengths from the available data.

By investigating the derivative of the spectra instead of the spectra, as shown in Figs. 7 and 9, the slowly varying but temperature-dependent difference-frequency absorption is suppressed. The approach is to use the derivatives to determine the mode strengths directly so that no background subtraction, with its inherent uncertainty, is needed. To quantify this method, we assume that the experimentally measured absorption coefficient $\alpha(\omega)$ in the region of an IR-active mode superimposed on a frequency-dependent broad-band absorption background can be written as the sum of two functions, $\alpha(\omega)=a(\omega)+b(\omega)$, where $a(\omega)$ describes a symmetric narrow absorption line and $b(\omega)$ describes the slowly varying difference-band background. In general, both $a(\omega)$ and $b(\omega)$ are functions whose exact analytical forms are not known, so that accurate fitting to the measured $\alpha(\omega)$ is difficult. Of interest here is the integrated strength of the absorption line, $a(\omega)$. In what follows, it is assumed that $b(\omega)$ is slowly varying in the frequency interval in which the variation of $a(\omega)$ is significant, i.e., that $d\alpha/d\omega \approx da/d\omega$; this has been shown to be the case here (compare Figs. 5 and 7). Now let the absorption line $a(\omega)$ be written as $a(\omega)=Sf(\omega)$, with $f(\omega)$ normalized such that

$$\int_{-\infty}^{\infty} f(\omega)d\omega \equiv 1 \ . \tag{22}$$

Then the absorption strength is S. If the signal-to-noise ratio of the data is large enough, then $da/d\omega \equiv S(df/d\omega)$ can be obtained from the measured $\alpha(\omega)$ by numerical differentiation of the spectra, which automatically eliminates the background function $b(\omega)$. The remaining challenge is to obtain the temperature dependence of S from the derivative spectra. As described below, a more indirect approach is required to obtain S from $da/d\omega$ than from $a(\omega)$.

In principle, S can be obtained simply from the shape of $da/d\omega$. For Voigt line shapes, the distance between the maximum and minimum abscissa values of this function is proportional to S/Γ^2, where Γ is proportional to the full width at half maximum of $a(\omega)$, while the distance between the corresponding ordinate values is proportional to Γ. Since both S and Γ are temperature dependent for the Ag^+ gap mode (though Γ is only weakly so), it is important to keep track of the changes in Γ. One problem with this technique is that it relies on only a small portion of the available data.

A way of using all of the available data in the derivative of a spectrum to determine the strength of a mode is to numerically integrate two quantities, namely,

$$I_1 \equiv \int_{\omega_0}^{\infty} \left[\frac{da}{d\omega} \right] d\omega \propto S/\Gamma \tag{23}$$

and

$$I_2 \equiv \int_{0}^{\infty} \left[\frac{da}{d\omega} \right]^2 d\omega \propto S^2/\Gamma^3 \ , \tag{24}$$

where ω_0 is the center frequency of the peak (which can be accurately determined for a symmetric line shape from the zero crossing of the derivative). From these results, the strength of the mode is $S \propto I_1^3/I_2$. The proportionality constant is $4/\pi^2$ for a Lorentzian line shape and $\sqrt{2}/\pi$ for a Gaussian one. For a Voigt line shape, which describes the experimental results reasonably well, the proportionality constant is determined by numerical analysis to vary between these two values, depending on the relative sizes of the Gaussian and Lorentzian contributions to the line shape. If the line shape were to change (e.g., with temperature) from being predominantly Lorentzian to being predominantly Gaussian, a maximum error of 10% would occur in the determination of the temperature dependence of the mode strength. However, in the present study, the experimental line shape is predominantly Lorentzian at all temperatures with only a small Gaussian contribution; thus this source of error is negligible.

The results of this method of analysis for the unperturbed KI:Ag^+ pocket gap mode are shown as the triangles in Fig. 11(a); they are seen to be in good agreement with the results obtained from the other analysis methods described above; hence, both data analysis approaches provide consistent results. Because of the unusual temperature dependence of the background absorption observed between the isotope and the unperturbed gap mode, shown in Fig. 10, we have not attempted to use the derivative method to reinvestigate the temperature dependence of the strength of the isotope mode.

IV. DISCUSSION

A. The isotope effect

There are two different ways of producing the Ag^+ gap-mode isotope effect: by changing the mass of the impurity or by changing the mass of one or more of the host-lattice ions in its vicinity. We now consider these possibilities in turn.

First, we consider the $^{107-109}Ag^+$ isotope effect for a "standard" gap mode, whose maximum amplitude is localized on the impurity ion. Since the two naturally occurring silver isotopes have nearly equal abundances, this would produce two peaks of nearly equal strengths, qualitatively similar to the KI:Cl^- isotope peaks shown in Fig. 5. The gap-mode strengths reported here are much too disproportionate to be consistent with this model.

Second, we consider changing the mass of a neighboring host-lattice ion. There are now two subcategories, since the maximum amplitude of the T_{1u} gap mode can be either on or away from the impurity site. We first fit our defect model to an on-site case, the observed KI:Cs^+ gap mode at 82.9 cm^{-1}. Since Cs^+ is larger than K^+, it is reasonable to assume that both δ and δ' are positive and that the fractional changes δ/k and δ'/k are in the range (0,1). Within this range, we find that the observed KI:Cs^+ gap-mode frequency is almost entirely determined by the defect–nearest-neighbor force constant change δ: varying δ'/k from 0 to 1 only changes δ/k from 0.304 to 0.298. This implies that the displacement pattern for this gap mode is peaked at the impurity, much like the T_{1u} 17.3-cm^{-1} KI:Ag^+ resonant-mode pattern shown in Fig. 1. In contrast to the large $^{41}K^+$ frequency shift predicted and observed here for the KI:Ag^+ pocket gap mode, our predicted $^{41}K^+$ (200) isotope shift for this "standard" 82.9-cm^{-1} KI:Cs^+ gap mode is less than 0.1 cm^{-1}. Furthermore, our predicted shift for this mode under *second*-neighbor [e.g., (110)] $^{41}K^+$ isotopic substitutions is even smaller, namely 0.008 cm^{-1}. These possible $^{41}K^+$ isotope shifts for the KI:Cs^+ gap mode are at least an order of magnitude smaller than the isotope shift reported here for the KI:Ag^+ pocket gap mode. Thus a sharply peaked amplitude at the defect site cannot explain our data.

In the second subcategory, the maximum amplitude of the T_{1u} gap mode is away from the impurity site, as occurs for the pocket modes. Suppose that the T_{1u} gap mode in KI:Ag^+ were an *isolated* pocket mode, i.e., that the predicted A_{1g} and E_g modes were not present. In this case, nondegenerate perturbation theory applies and a $^{41}K^+$ isotopic substitution on one of the defect's (200) fourth neighbors produces a pocket isotope mode. The largest possible frequency shift occurs for the case of a T_{1u} pocket mode whose displacements are entirely localized on the ($\pm$200) sites. In this extreme limit, the isotopic frequency shift would be -1.1 cm^{-1}. Moreover, the relative absorption strengths for isolated modes are determined solely by statistical and index of refraction factors.[18] In the present case, an isolated T_{1u} pocket gap mode with its displacement pattern strongly peaked on the fourth neighbors would produce an isotope IR-absorption line of relative strength $S_1/S_o \approx 0.15$. This is higher than the measured value by a factor of 4 (0.15 compared with 0.04) and goes with a maximum frequency shift which is too small (-1.1 cm^{-1} compared with the measured -1.7 cm^{-1}). Although these two discrepancies are in opposite directions, they are nevertheless within an order of magnitude. Hence this model at least has roughly the right qualitative behavior.

As noted at the end of Sec. II, our predicted and measured pocket-gap-mode isotope splitting and the absorption strength of Table IV are in good agreement. Unlike the *isolated* pocket-mode model discussed in the preceding paragraph, an essential ingredient of our model is its inclusion of *all* of the nearly degenerate pocket modes of A_{1g}, E_g, and T_{1u} symmetries. It is the mixing of these modes by the isotopic perturbation which results in the good quantitative agreement exhibited in Table IV. We emphasize that our predictions involved no new or adjustable parameters; rather they are direct consequences of our perturbed harmonic model for the on-center configuration. This good agreement is strong evidence for the existence of the unusual nearly degenerate pocket gap modes. The evidence is even stronger considering that our observed isotope spectra *cannot* be explained by a harmonic model if the 86.2 cm^{-1} T_{1u} gap mode were to have a more typical local-mode displacement pattern peaked at the impurity. In summary, neither the impurity-peaked gap mode explanation nor the isolated pocket-gap-mode explanation can reproduce quantita-

tively the measured frequency shift and strength for the KI:Ag^+ isotope mode.

In view of the good agreement between our pocket-isotope-mode predictions and experiment, the absence of fitting parameters or extensions (e.g., anharmonic corrections) in our model calculations, and the failures of the alternative explanations noted above, we regard the existence of the unusual pocket gap modes in KI:Ag^+ as being established.

We should note, however, that it would be misleading to conclude from this success that our two-parameter harmonic-defect model can reproduce the *entire* far-IR spectrum observed for the KI:Ag^+ system. Figure 12 shows the measured low-temperature absorption (curve *A*) over the frequency region below the reststrahl. Also shown is our calculated impurity-induced absorption (curve *B*) over the same region for the present model. For clarity, the gap-mode δ function is not shown. We have demonstrated here that our perturbed harmonic phonon model gives a good account of the positions and strengths of the resonant mode and the pocket gap modes, as well as of the pocket-mode isotope effect, but we see from Fig. 12 that it does not simultaneously account for the frequency dependence or strength of the broad-band absorption in the acoustic-phonon region. This could be due to neglected anharmonic or electronic deformation effects involving the Ag^+ ion, or to our neglect of static relaxation effects beyond the defect's fourth-nearest neighbors.

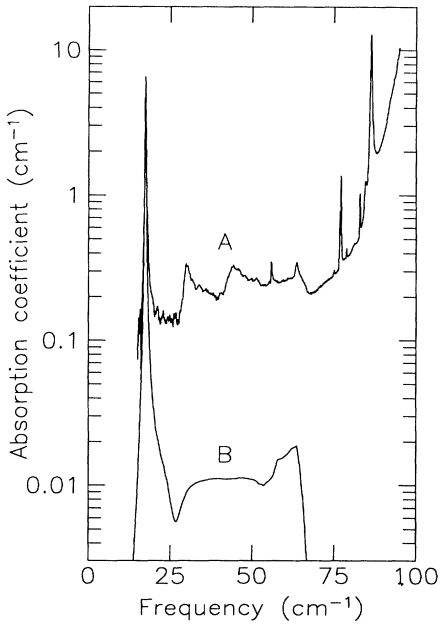

FIG. 12. Impurity-induced absorption coefficient of KI:Ag^+ vs frequency. Curve *A*: Far-IR absorption coefficient of KI:Ag^+ below the optical-phonon region, at 1.7 K. The dominant features are the KI:Ag^+ resonant and gap modes at 17.3 and 86.2 cm^{-1}, respectively, and the gap modes due to KI:Cl^- at 76.8 and 77.1 cm^{-1} and KI:Cs^+ at 82.9 cm^{-1} (Cl^- and Cs^+ are present as natural impurities). Additional weak features due to KI:Ag^+ are at 30, 44, 55.8, 63.6, and 84.5 cm^{-1}; all are associated with the on-center configuration of the Ag^+ impurity. The instrumental resolution is 0.1 cm^{-1}. Curve *B*: the calculated absorption coefficient according to the two-parameter harmonic model described in the text. The gap-mode δ function is not shown. Note that the structure in the acoustic spectrum for curve *A* is not associated with density of states features in curve *B*.

B. Temperature dependence

Early measurements of the temperature dependence of the strengths of the resonant mode and the gap mode produced similar dependences; however, because of the difference-band absorption, the errors in determining the strength of the gap mode were much larger than for the resonant mode.[5] It has been proposed,[5] and demonstrated to some extent,[7] that the temperature dependence should be the same for all optical probes which monitor the Ag^+ defect system if it is a consequence of the population in the on-center configuration. If a difference were found between the temperature dependences of the resonant and gap modes, the two-configuration (on-center—off-center) model could be eliminated. On the other hand, if there is a common temperature dependence for these modes, it is of interest to determine its functional form since this provides a direct measure of the entropy available in the off-center configuration.[5] Finally, we need to determine whether the newly discovered pocket isotope mode, which has a different local defect symmetry and hence can be thought of as a different defect, shares this common temperature dependence.

The problem in determining the strength vs temperature for both the 86.2-cm^{-1} pocket gap mode and the pocket isotope mode is complicated by the presence of the strongly temperature-dependent intrinsic difference-band absorption background. However, the good signal-to-noise ratio obtained by averaging with the scanning interferometer allows examination of the derivative of the absorption spectra in addition to the spectra themselves, so there are two different ways to analyze the temperature-dependent data and check the self-consistency of the results. We find that the difference-band subtraction method and the derivative method, described in Secs. III B 1 and III B 2, give identical temperature dependences for the pocket-gap-mode strength, and that this temperature dependence is the same as that found earlier for the resonant mode.

Because of the relative weakness of the pocket isotope mode and the presence of other weak unexplained temperature-dependent features in the same frequency region (see, for example, Fig. 10), it is not possible to use the derivative method to analyze the strength of the isotope mode with any confidence. However, the difference-band background subtraction method does produce a curve similar to the temperature dependence of the resonant mode, with errors such that these two curves could, in principle, be identical.

Another new result is the unusual temperature dependence of the high-temperature mode at 78.6 cm^{-1}, which had previously been identified with the off-center

configuration.[5] The absorption difference results (Fig. 10) show that although the strength of this mode grows at low temperature, it attains its maximum value at a temperature of ~ 12 K, much smaller than that associated with the disappearance of the on-center configuration. It now appears that this high-temperature mode may, in fact, not be associated with the off-center configuration of the Ag^+ ion but rather with another configuration available to the Ag^+ at intermediate temperatures.

V. CONCLUSIONS

A. Pocket modes

The low-temperature dynamics of KI:Ag^+ are well described by a nearly unstable perturbed harmonic model which includes substantial force-constant weakening. The most striking prediction of our model is the existence of three nearly degenerate pocket gap modes of different symmetries: A_{1g}, E_g, and T_{1u}. All three of these modes have very unusual displacement patterns, with amplitudes strongly peaked on the impurity's fourth-nearest neighbors. The T_{1u} pocket gap mode is observed in IR absorption. The even-parity A_{1g} and E_g pocket gap modes should be Raman active, but have Raman intensities too weak to be observed. However, naturally occurring $^{41}K^+$ isotopes present at the impurity's fourth-nearest-neighbor sites mix these nearly degenerate gap modes, producing new pocket isotope modes with predicted frequencies and relative intensities in good agreement with the high-resolution IR measurements reported here. Our results directly confirm the existence of these nearly degenerate modes and their unusual displacement patterns.

The A_{1g} and E_g pocket modes involve no motion of the Ag^+ impurity and are hence independent of the defect mass. The T_{1u} pocket mode involves a negligibly small defect displacement and thus should be essentially independent of the defect mass. Indeed, if we keep the force-constant changes δ and δ' fixed in our model, and vary the defect mass change from $\Delta m = 68.9$ amu to $\Delta m = 0.0$ (corresponding to $m_{Ag^+} \rightarrow m_{K^+}$), we find that the T_{1u} pocket-mode frequency changes by less than 0.04%. Furthermore, the pocket modes were found to be present for all values of δ and δ' along the T_{1u} 17.3-cm^{-1} resonance-mode curve of Fig. 3, for $\delta' \leq -0.2$. Thus the nearly degenerate pocket gap modes are a general feature of our perturbed harmonic model for any cation impurity which introduces these large force-constant weakenings.

The ubiquity of these modes for our KI:Ag^+ defect model suggests that pocket modes might be a general feature of a class of impurity-host systems. The substantial force-constant weakening in our model is due to the presence of the low-frequency T_{1u} resonance mode at 17.3 cm^{-1}. This suggests that pocket gap modes might be a general feature of systems with low-frequency resonance and large host-crystal phonon gaps. To address this possibility, we examined the system NaI:Cl^-, which has a wide phonon gap and an even lower-frequency T_{1u} resonance, at 5.4 cm^{-1}.[19,20] We applied our model to this system and found that for all force-constant changes consistent with the 5.4-cm^{-1} resonance, the predicted gap-mode displacement patterns are *localized at the impurity,* in sharp contrast to the displacement patterns for the pocket modes in KI:Ag^+. This in turn suggests that another key requirement for the existence of the pocket modes is that the light host-lattice constituent should occur at the impurity's fourth-nearest neighbors. To test this, we considered the hypothetical "inverse" systems NaI:Ag^+ and KI:Cl^-, with force-constant changes obtained by assuming the simultaneous presence of a T_{1u} resonant mode near zero frequency and a T_{1u} localized mode in the gap. These calculations yielded pocket modes for the former case, but not for the latter, consistent with the above conjecture. Hence, pocket modes appear to be a general feature of a class of impurity-lattice systems.

B. Importance for KI:Ag^+

The experimental confirmation of the pocket modes in KI:Ag^+ involved a careful analysis of their temperature behavior and concentration dependence in high-resolution far-IR-absorption spectra, together with a detailed study of the changes of their IR spectra due to the naturally occurring presence $^{41}K^+$ isotopes in our samples. The observed dependence on Ag^+ concentration is linear, and the qualitative temperature behavior of both the 86.2-cm^{-1} IR gap-mode peak and its isotope satellite is the same as that found for the 17.3-cm^{-1} IR resonant mode, for the 16.1-cm^{-1} Raman mode, for the electronic Ag^+ absorption, and in dielectric loss measurements. To determine quantitatively the experimental gap- and isotope-mode peak relative positions and intensities needed for comparison with our model predictions, we employed a careful fitting procedure that included a subtraction of the temperature-dependent background absorption. The resulting comparison with our model predictions was the key element in confirming the unusual pocket nature of the gap modes in KI:Ag^+.

Having thus established that the displacements for the 86.2-cm^{-1} IR gap mode in KI:Ag^+ are essentially confined to just the host-crystal (200) family of ions, as opposed to the case for the low-frequency 17.3-cm^{-1} resonant mode, whose displacements are peaked on the Ag^+ and its nearest neighbors in our model, it was realized that the quantitative temperature dependences of the strengths of these two modes can provide important complementary information on the participation of the Ag^+ impurity's surrounding ions in this system's anomalous thermally driven (on$\rightarrow$off)-center transition of the Ag^+ ion. Unfortunately, despite the careful fitting procedure used to determine the gap- and isotope-mode peak relative positions and intensities, the experimental uncertainties in the temperature dependence of the strengths remained much larger than those for the 17.3-cm^{-1} resonant mode, owing to the temperature-dependent background in the experimental gap-mode region. Accordingly, the new derivative technique described here was developed, leading to large reductions in the experimental uncertainties. The important result of this analysis is that both the low-frequency IR resonant mode and the strong pocket IR gap mode disappear at *identical* rates

with temperature in the range 0–25 K, even though the dynamics of each involve different regions of the defect space. Since the mode frequencies are nearly temperature independent over this temperature interval, it appears that these two nearly harmonic modes simply monitor, in different spatial regions, the population of the on-center configuration. Thus the present study has not only confirmed the unusual pocket nature of the gap modes in the low-temperature on-center configuration of KI:Ag^+, it has also allowed us to use this property to reveal that the thermally driven instability in this system involves the *entire* coupled defect-host system in the impurity region.

ACKNOWLEDGMENTS

Discussions with C. E. Mungan have been very helpful. The research by K.W.S. and J.B.P. was supported by NSF-DMR-9014729 and DMR-9012143. J.B.P. gratefully acknowledges the support of the Alexander von Humboldt Foundation during a portion of this work. The research by A.R. and A.J.S. was supported by NSF-DMR-8918894 and ARO-DAAL0390G0040. We also acknowledge the crystal growing facility support through the Cornell Materials Science Center under NSF-DMR-8818558-A02.

---

*Permanent address.

[1]A. A. Maradudin, E. W. Montroll, G. H. Weiss, and I. P. Ipatova, *Theory of Lattice Dynamics in the Harmonic Approximation,* 2nd ed., Solid State Physics Supplement, Vol. 3 (Academic, New York, 1971).

[2]A. S. Barker, Jr. and A. J. Sievers, Rev. Mod. Phys. **47**, Suppl. 2, S1 (1975).

[3]H. Bilz, D. Strauch, and R. K. Wehner, *Handbuch der Physik* (Springer-Verlag, Berlin, 1984), Vol. XXV, Pt. 2d.

[4]K. W. Sandusky, J. B. Page, A. Rosenberg, C. E. Mungan, and A. J. Sievers, Phys. Rev. Lett. **67**, 871 (1991).

[5]A. J. Sievers and L. H. Greene, Phys. Rev. Lett. **52**, 1234 (1984).

[6]S. B. Hearon and A. J. Sievers, Phys. Rev. B **30**, 4853 (1984).

[7]J. B. Page, J. T. McWhirter, A. J. Sievers, H. Fleurent, A. Bouwen, and D. Schoemaker, Phys. Rev. Lett. **63**, 1837 (1989).

[8]R. D. Kirby, Phys. Rev. B **4**, 3557 (1971).

[9]J. B. Page, Phys. Rev. B **10**, 719 (1974).

[10]M. V. Klein, in *Physics of Color Centers,* edited by W. B. Fowler (Academic, New York, 1968), p. 455.

[11]R. T. Harley, J. B. Page, and C. T. Walker, Phys. Rev. B **3**, 1365 (1971).

[12]U. Schröder, Solid State Commun. **4**, 347 (1966).

[13]Since there are isotope modes within 0.2 cm^{-1} of the unperturbed T_{1u} pocket gap mode, our calculated unshifted T_{1u} pocket-gap-mode strength includes contributions from these unresolvable modes, as explained in the text.

[14]A. Rosenberg, C. E. Mungan, A. J. Sievers, K. W. Sandusky, and J. B. Page, Phys. Rev. B **46**, 11 507 (1992).

[15]S. P. Love, W. P. Ambrose, and A. J. Sievers, Phys. Rev. B **39**, 10 352 (1989).

[16]R. D. Kirby, A. E. Hughes, and A. J. Sievers, Phys. Rev. B **2**, 481 (1970).

[17]B. Di Bartolo, *Optical Interactions in Solids* (Wiley, New York, 1968), p. 366.

[18]D. Bäuerle, *Vibrational Spectra of Electron and Hydrogen Centers in Ionic Crystals,* Springer Tracts in Modern Physics Vol. 68 (Springer-Verlag, Berlin, 1973), p. 130.

[19]B. P. Clayman, I. G. Nolt, and A. J. Sievers, Solid State Commun. **7**, 7 (1969).

[20]J. B. Page and K. G. Helliwell, Phys. Rev. B **12**, 718 (1975).